J Solid State Electrochem (2010) 14:1585–1594
DOI 10.1007/s10008-009-0987-y

ORIGINAL PAPER

Structural and electrochemical behavior of Mn–V oxide synthesized by a novel precipitation method

Xiaoying Xie · Wenwen Liu · Luyang Zhao · Chengde Huang

Received: 25 August 2009 / Revised: 29 November 2009 / Accepted: 4 December 2009 / Published online: 22 December 2009

Abstract Manganese–vanadium oxide had been synthesized by a novel simple precipitation technique. Scanning electron microscopy, X-ray diffraction, Brunauer–Emmett–Teller, thermogravimetric analysis/differential scanning calorimetry, and X-ray photoelectron spectroscopy were used to characterize Mn–V binary oxide and δ-MnO_2. Electrochemical capacitive behavior of the synthesized Mn–V binary oxide and δ-MnO_2 was investigated by cyclic voltammetry, galvanostic charge–discharge curve, and electrochemical impedance spectroscope methods. The results showed that, by introducing V into δ-MnO_2, the specific surface area of the mixed oxide increased due to a formation of small grain size. The specific capacitance increased from 166 F g^{-1} estimated for MnO_2 to 251 F g^{-1} for Mn–V binary oxide, and the applied potential window extended to −0.2–1.0 V (vs. saturated calomel electrode). Through analysis, it is suggested that the capacitance performance of Mn–V binary oxide materials may be improved by changing the following three factors: (1) small grain and particle size and large activity surface area, (2) appropriate amount of lattice water, and (3) chemical state on the surface of MnO_2 material.

Keyword Mn–V binary oxide · Supercapacitor · Chemical precipitation · Chemical state

X. Xie · W. Liu · L. Zhao · C. Huang (✉)
Department of Applied Chemistry, School of Chemical Engineering and Technology, Tianjin University, Tianjin 300072, People's Republic of China
e-mail: cdhuang@tju.edu.cn

Introduction

With the rapid development of economy and growth of population, it is urgent to seek a new type of energy, which has the advantages of safety, high efficiency, non-pollution, renewable, and economical performance. Supercapacitor, which fills the gap between batteries and conventional dielectric capacitors, is a new type of energy storage device. Supercapacitor has attracted wide attention in recent years due to its attractive features, such as high specific capacitance, excellent pulse charge–discharge property, very long cycle life, wide temperature range of operation and environment-friendly character [1]. In general, supercapacitors can be classified into two categories depending on the charge storage mechanism: the electric double-layer capacitors and the redox supercapacitors or pseudocapacitors (PCs). The former is based on charge separation at the electrode/solution interface, whereas the latter is based on the Faradic reactions occurring at the electrode.

Recently, much attention has been focused on the development of the new electrode materials and new electrolyte for PCs [2–6]. Manganese dioxide is a potential candidate as an electrode material for supercapacitor among these transition metal oxides due to low cost, abundant resources, and the faradic pseudocapacitance exhibited similar to ruthenium oxide (RuO_2) [3, 4].

Many studies indicate that amorphous hydrous manganese dioxide has shown high specific capacitance beyond other transition metal oxides, such as nickel oxide (NiO) [5], vanadium pentoxide (V_2O_5) [6], but compared with hydrous ruthenium oxide (RuO_2), its capacitor performance is still far from satisfactory.

Recently, the capacitance of manganese dioxide is improved by the following two ways: (1) the crystal

structure, the adsorbed water content, specific surface area, and surface morphology of manganese dioxide is adjusted by changing synthesized methods and reaction conditions. There are a variety of approaches, including hydrothermal method [7], sol–gel [8], microemulsion method [9], solid state reaction [10], sonochemistry method [11], and so on. The reaction conditions mainly include reaction time, pH, heat-treatment temperature, precursors, and so on [2]. The second element is introduced into manganese dioxide to prepare the composite materials, for example Mn/Ni, Mn/Pb [12], etc. Adding the second element not only helps to achieve the complementation in the performance of materials but also to influence the physic and chemical properties of manganese dioxide. In addition to Mn/Ni and Mn/Pb, there are studies on the capacitance performance of Mn/Fe [13] and Mn/Co [14].

In these doped elements, vanadium seems very interesting because amorphous V_2O_5 possesses high capacitance in neutral electrolyte and the applied potential range reveals no significant difference between V_2O_5 and MnO_2. Nakayama et al. [15] reported that thin films of mixed manganese (mainly 4^+) and vanadium (5^+) oxides were obtained by electrodeposition method. Voltammetric response of the heat-treated Mn–V oxide film in borate solution was enhanced with increasing the number of potential cycles, and the steady-state current was much larger than that of pure manganese oxide. However, electrodeposition method only obtains the thin film sample, then the thin film sample needs to be heat treated under vacuum at 300 °C, so the subsequent process is complicated. Therefore, it is necessary to find the new methods of preparing Mn–V oxide and investigate the effect of adding vanadium element on the hydrous state and crystalline structure of MnO_2.

In this study, an attempt was made to synthesize mixed oxide based on MnO_2 by a new simple chemical-precipitation method. The physical characteristic and electrochemical behavior of Mn–V oxide and δ-MnO_2 were investigated and compared by various techniques including X-ray diffraction (XRD), scanning electron microscopy (SEM), thermogravimetric analysis (TGA), differential scanning calorimetry (DSC), X-ray photoelectron spectroscopy (XPS), cyclic voltammogram (CV), electrochemical impedance spectroscopy (EIS) and galvanostatic charge/discharge.

Experimental

Synthesis of Mn–V binary oxide

All the chemicals used were of analytical grade, and they were used without further purification. All solutions were prepared in double-distilled water. The amorphous vanadium oxide ($V_2O_5 \cdot nH_2O$) was prepared by a process described in [16]. A certain amount of V_2O_5 powder [corresponding to $n(MnO_2)/n(V_2O_5)=3:1$] was calcined at 800 °C for 20 min to obtain product. The heating rate is 10 °C/min. The resulting product was poured into a beaker of distilled water and stirred for 30 min, filtered to obtain a browned viscous sol. While the solution was stirred, $KMnO_4$ solution was added, and then they were mixed with $MnSO_4$ solution and stirred continuously for 6 h. A dark-brown precipitate thus formed and was washed several times with distilled water, centrifuged, and dried at 70 °C in air for 12 h. The concentration of $MnSO_4$ was 0.15 mol L^{-1}, and the initial molar ratio of $KMnO_4$/$MnSO_4$ was 2:3. The pure MnO_2, by maintaining the molar ratio of $KMnO_4/MnSO_4$ at 2:3, was also prepared for comparison. The subsequent preparative procedures were similar to that of the Mn–V binary oxide as mentioned above.

Materials characterization

The X-ray diffraction measurements were performed on a Rigaku D/max2500V X-ray diffractiometer with a Cu K_α (λ=1.5418 Å) radiation source, from 10° to 90°(2θ), using steps of 0.13°(2θ) and a step time of 1 s. The surface morphologies were obtained by a field-emission scanning electron microscope (FE-SEM, Hitachi S-4800-type). TGA and DSC were recorded in the temperature range from ambient to 1,000 °C in nitrogen atmosphere at a heating rate of 10 °C/min using Stetsys evolution-16 tester. The Brunauer–Emmett–Teller (BET) surface area were measured by the nitrogen gas adsorption–desorption method at 77 K using a Quantachrome surface area analyzer model Nova-2000. In this work, XPS (PHI 1600 XPS spectrometer, USA) was used to characterize the chemical composition of the surfaces. The XPS spectra were recorded with Mg K_α radiation as an excitation source. The analyses were performed at 250 W. The vacuum in the chamber maintained around 2×10^{-9}Torr during the measurement. At the same time, an electron gun was employed to compensate the surface positive charge. The area of the samples was relatively large (0.8 mm^2), and the estimated sampling depth was around 2–5 nm. The survey spectra were performed with pass energy of 187.85 eV at a step of 0.5 eV, and the high resolution spectra were collected with pass energy of 29.35 eV at a step of 0.125 eV. The binding energy scales for the samples were corrected by referencing the C1s binding energy to graphite carbon at 284.6 eV. To determine the quantification of the elemental concentrations and the binding states, curve fitting was performed using Gaussian–Lorentzian line shapes after a linear background subtraction.

Preparation of electrode

The working electrode was prepared by inserting an active paste, which contained 75 wt.% synthesized MnO_2 or Mn–V binary oxide, 20 wt.% acetylene black, and 5 wt.% polytetrafluorene-ethylene binder, into a nickel foam substrate. Small amount of ethanol was added to the mixture to produce more homogeneous paste by ultrasound for 30 min. The mixture dispersion was hand-brushed to nickel foam. The electrode was dried at room temperature and pressed.

Electrochemical measurement

Eletcrochemical characterization was carried out in a conventional three-electrode cell. Platinum foil and saturated calomel electrode (SCE) were used as counter and reference electrode, respectively. Cyclic voltammetry (CV) and galvanostatic charge–discharge studies were performed using a CHI 660B electrochemical workstation (Chenhua Inc., Shanghai, China) between −0.2 and 1.0 V (vs. SCE) in a 0.5 mol L^{-1} Na_2SO_4 electrolyte for Mn–V binary oxide. The electrochemical measurements of pure MnO_2 were performed in the potential range of 0.0 to 1.0 V (vs. SCE). The specific capacitance can be calculated from the following equation [17]:

$$C_m = \frac{i\Delta t}{m\Delta V} \tag{1}$$

where i is the galvanostatic charge-discharge current density applied, $(\Delta V/\Delta t)$ is the slope of the charge–discharge plot, and m is the mass of the active materials (MnO_2 or Mn–V binary oxide). The ac impedance measurements were conducted by means of a potentiostat (CH Instruments CHI 660B, China) under open-circuit conditions. An ac perturbation amplitude of 5 mV vs. the open-circuit potential was applied in the frequency range between 100 kHz and 50 mHz.

Results and discussion

Figure 1 shows the surface morphology of Mn–V binary oxide and MnO_2 at different magnification. It can be seen that the large space and small agglomerates will be formed between the particles of Mn–V binary oxide, and the particles are arranged and interact with each other and mingle to form the network structure. The abundant cellular structure has been shown on the surface of Mn–V particles. This structure is not only beneficial to the diffusion of ions from the electrolyte to all available pores of the electrode, leading to a complete insertion reaction of H^+ or alkali metal cations in the electrolyte, but also beneficial to the adsorption/desorption of cations in the electrolyte on the surface of composite electrode. For pure MnO_2, it can be observed that the particles are close together. Space between particles of the sample is relatively small, and the mosslike structure on the surface is less; therefore, the active surface of MnO_2 particles is probably less than that of Mn–V binary oxide.

Figure 2 shows the XRD patterns of pure MnO_2 and Mn–V binary oxide. The two main broad reflection at 2θ= 37.0° and 66.2° indicate that both samples are poorly crystalline MnO_2 and the profiles seem to correspond to some peaks of δ-MnO_2 (JCPDS no. 52-0556). This XRD profile is consistent with the report by Ragupathy et al. [18] that the nano-MnO_2 is in a partially crystalline state, and the diffraction peaks locate at 2θ values of 37.0° and 66.0°, respectively. In order to study the crystal structure of MnO_2 with amorphous nature, Ragupathy et al. [18] have performed Mn K-edge XANES analysis on the obtained nano-MnO_2. Their results demonstrate that the obtained sample has δ-MnO_2-type structure locally even though it is nearly X-ray amorphous. Therefore, the MnO_2 obtained in our work also has δ-MnO_2-type local structure. In addition, there is no diffraction peak of V_2O_5 in curve a, but the Bragg angle of MnO_2 diffraction peak is smaller than that of pure MnO_2(curve b), which meant that the crystalline V_2O_5 did not form in Mn–V binary oxide but probably widely distribute in layered structure δ-MnO_2. It is also observed that the intensity of diffraction peaks of pure δ-MnO_2 is stronger and sharper than that of Mn–V binary oxide. This shows that the crystalline degree of pure δ-MnO_2 is higher, and the grain size is larger. Cullity and Stock [19] indicate that X-ray diffraction can also disclose crystallinity size of amorphous and semi-amorphous solids, usually by means of the Scherrer's equation for line broadening and preferred orientation. The peak around 2θ=37.0° were used to calculate the crystalline grain size of MnO_2 according to the Scherrer's equation (B is the width of the diffraction peak at half height in radians, λ is the wavelength of the X-rays used (1.54056 Å), and θ is the angle at the position of the peak maximum).

$$d = (0.9\lambda)/(B \times \cos\theta)$$

The average size of pure δ-MnO_2 and Mn–V binary oxide calculated from the Scherrer's equation is about 15 and 10 nm, respectively. Because the structure of Mn–V oxide is poorly crystalline and contains an amorphous part, the crystalline grain size is estimated value due to the error. The results show that the addition of V_2O_5 is in favor of forming the small crystalline grain size MnO_2 and probably leads to possess higher specific surface area. N_2 adsorption–desorption studies were performed to determine the specific surface area of materials. The BET surface area was found to be 191.2 and 118.1 m^2g^{-1} for Mn–V binary oxide and

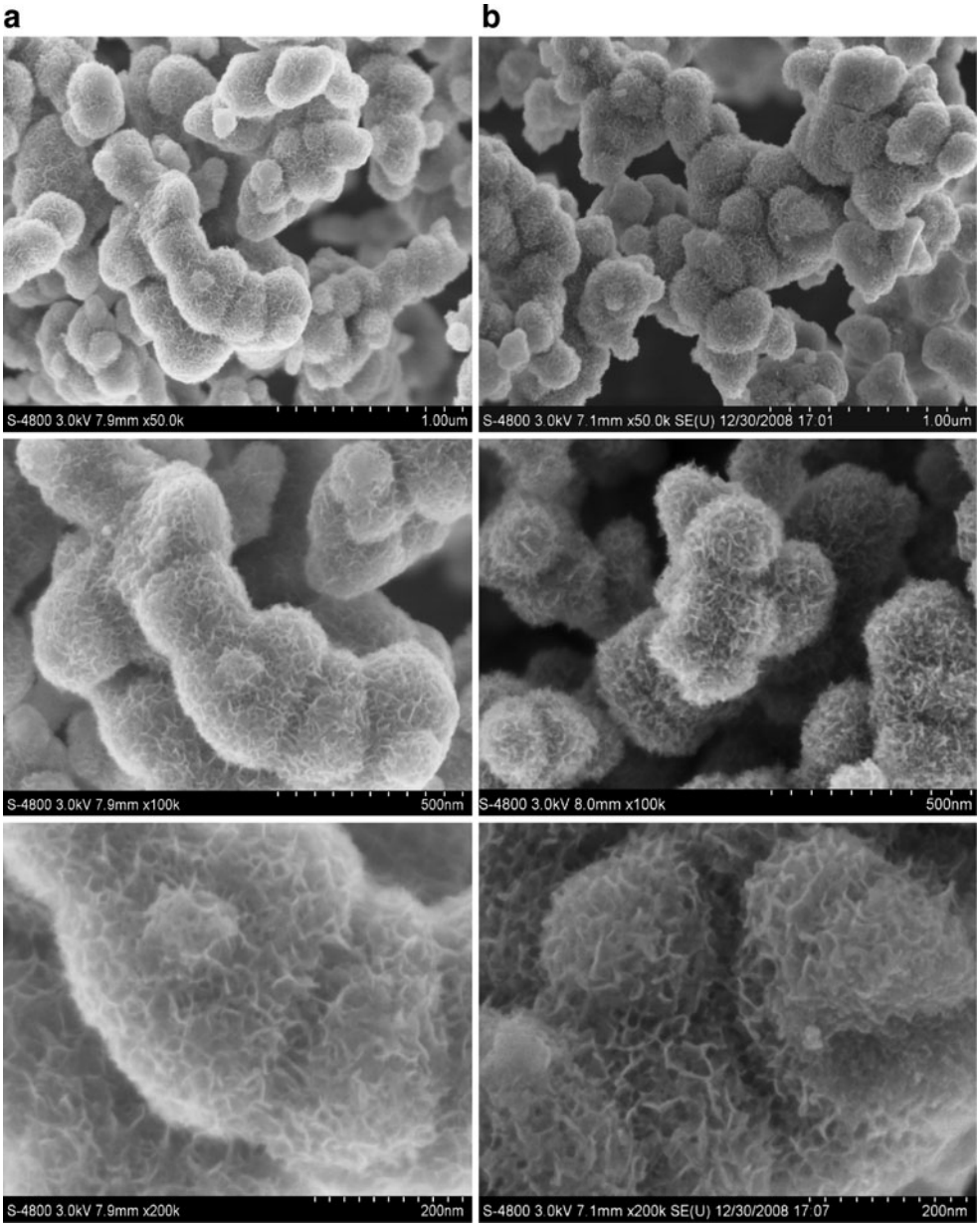

Fig. 1 FE-SEM images of sample MnO_2 (**a**) and Mn–V binary oxide powder (**b**)

δ-MnO_2, respectively. This conclusion is consistent with the result of XRD and SEM.

The reason for this phenomenon may be related to the preparation of composite materials. In the preparation process, the $KMnO_4$ primarily were adsorbed on the particles of small amorphous V_2O_5 sol. Then, $KMnO_4$ reacted with $MnSO_4$ to produce MnO_2. Therefore, in the formation process of final products, the V_2O_5 sol particle may play a role of carrier, and many small MnO_2 crystals were precipitated on the V_2O_5 sol particle. According to the previous report by different authors [2, 20], we conclude that the interaction exists between V_2O_5 and MnO_2. On one hand, the electron transfer probably appears between V_2O_5 and MnO_2; on the other hand, the growth form of MnO_2 crystal is affected by V_2O_5. Thus, compared with pure δ-MnO_2, the changes of morphology and grain size of Mn–V binary oxide can be observed.

TGA and DSC thermograms of Mn–V binary oxide and δ-MnO_2 powders are shown in Fig. 3a and b, respectively. The δ-MnO_2 displays the weight loss of 8.7 wt.% below 500 °C and endotherm around 113 °C, which corresponds to dehydration of the powders. Additional weight loss of 1.6 wt.% and exotherm around 508 °C could be attributed to the loss of oxygen in the MnO_2 lattice [21, 22]. Small weight loss and endotherm at 755 °C correspond to the phase transition from MnO_2 to Mn_2O_3 [23, 24]. Figure 3a presents the TG/DSC curves of Mn–V binary oxide. Strong endothermic peak were observed below 100 °C due to a loss of water, which was physically adsorbed. As temperature increases, only Mn–V binary oxide shows another

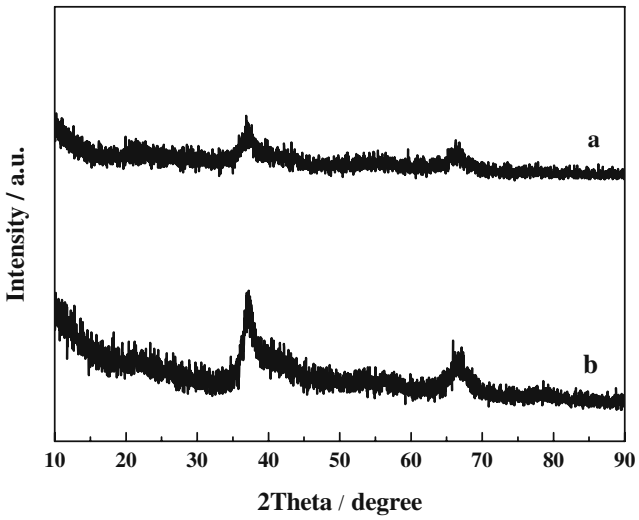

Fig. 2 XRD patterns of **a** Mn–V binary oxide and **b** pure MnO_2

small weight loss (0.6 wt.%) and an endothermic peak caused by the crystallization of amorphous V_2O_5 at approximatly 287 °C [25]. Two endothermic peaks around 478 and 700 °C with more weight losses also can be observed. The endothermic peak around 478 °C might be attributed to the transformation from γ-MnO_2 to the more stable Mn_2O_3 phase, and another endothermic peak around 722 °C is associated with the conversion from Mn_2O_3 to Mn_3O_4 phase under nitrogen gas accompanied by dissipation of oxygen gas. Comparing Fig. 3a and b, it can be seen that the TG/DSC curves of Mn–V binary oxide are different because V_2O_5 is added. Firstly, the weight loss for Mn–V binary oxide is 5.2 wt.% below 287 °C. Secondly, an endothermic peak around 287 °C is observed. In addition, the temperature of exothermic peak moves from 508 to 478 °C due to the existence of V_2O_5. Thirdly, the temperature of phase transition for MnO_2 in Mn–V binary oxide is decreased from 755 to 722 °C. Based on these results, it is reasonable to assume that both the change in the crystalline structure and the mixed oxide decomposition process contribute to the change of capacitance in the case of Mn–V mixed oxide.

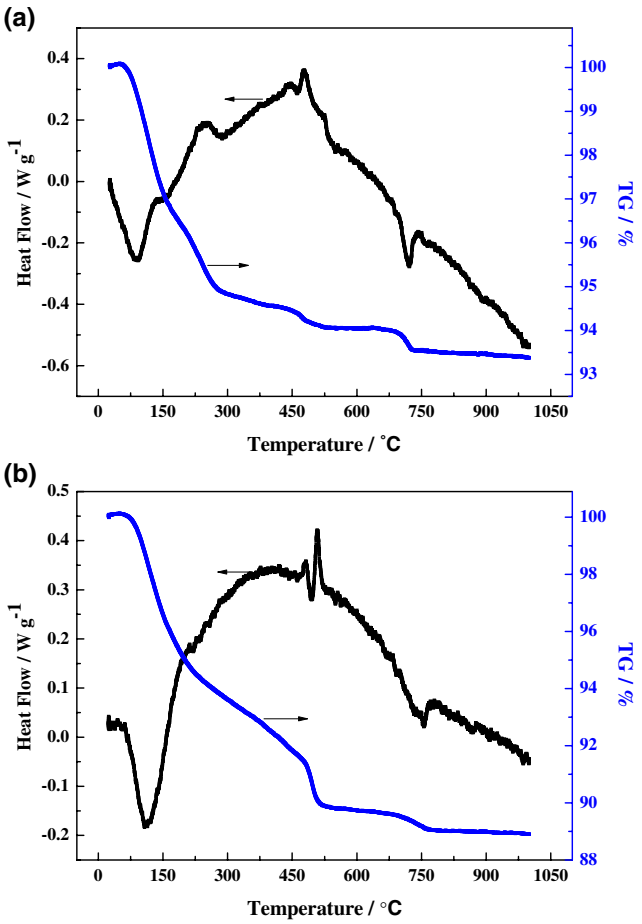

Fig. 3 TGA and DSC curves of **a** Mn–V binary oxide and **b** δ-MnO_2

XPS is an excellent technique to understand the oxidation state of the transition metal ion and the relative composition of the synthesized material. X-ray photoemission spectra of MnO_2-type compounds exhibit characteristic peaks near 642, 653.5, 529, and 85 eV, corresponding respectively to Mn 2p3/2, Mn 2p1/2, O 1 s, and Mn 3 s energetic levels [26–32]. It has been reported in Chang et al. [28] and Strohmeier and Hercules [33] that the binding energies of Mn 2p3/2 electron for Mn^{3+} and Mn^{4+} are 641.6 and 642.6 eV, respectively. The analytical results shown in Fig. 4 indicate that these oxides are probably composed of both trivalent and tetravalent manganese oxides. From Fig. 4 (insert), it also can be seen that the binding energy at 516.3 eV typical of V 2p3/2 was detected for Mn–V binary oxide. The literature data [34] show that the binding

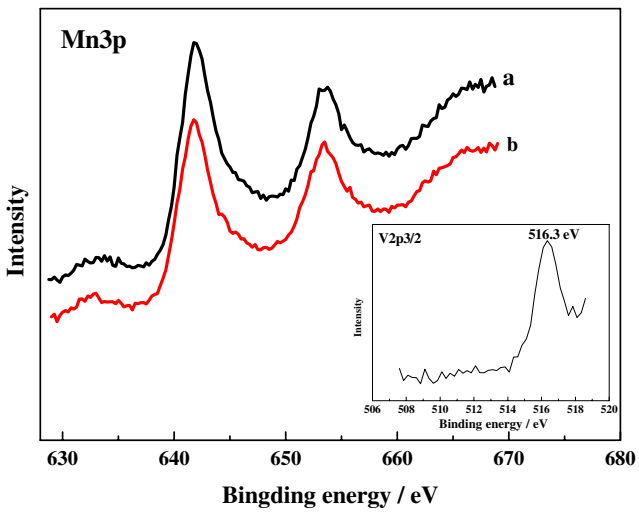

Fig. 4 XPS Mn 2p spectra of **a** Mn–V binary oxide and **b** δ-MnO_2. *Insert* X-ray photoelectron detailed spectra of V 2p3/2 in Mn–V binary oxide

energy for V^{4+} in VO_2 is between 516.2 and 516.4 eV. Therefore, the observed values indicate that the vanadium is present on the surface of Mn–V binary oxide investigated in the 4^+ valence form, as VO_2.

Earlier studies have shown that the localized positive and negative charge distribution on irradiation of X-rays on nonconductive samples, such as MnO_2 prepared in the present study, leads to the broadening or tailing of peaks at lower binding energy causing difficulty in accurately determining the valence state of Mn only from the Mn 2p3/2 peak [26, 35]. They have overcome this difficulty by analyzing O1s and Mn 3s spectra and by determining the splitting width of Mn 3s peaks and compared with the standard [27, 35, 36]. From Fig. 5, it is seen that the Mn 3-s peak of δ-MnO_2 are at binding energies 83.47 and 88.53 eV, and the peak separation energy is 5.06 eV. This value is slightly higher than that reported for δ-MnO_2 and is consistent with the presence of Mn(III) in the surface of δ-MnO_2 [26, 27, 36]. For Mn–V binary oxide powder, the energy slitting of Mn 3 s is 5.5 eV. This value is consistent with that reported for Mn_3O_4 (5.3–5.5 eV) [26, 27, 36]. Thus, it is clear that the surface oxidation state of MnO_2 will change by adding V_2O_5.

The O 1s spectra of δ-MnO_2 and Mn–V binary oxide are also shown in Fig. 6. The obtained spectra were deconvoluted into the manganese oxide peak (Mn–O–Mn) at 529.6 eV, the vanadium oxide peak at 530.3 eV, the hydroxide (Mn–O–H) peak at 531.57 eV and water molecule (H–O–H) peak at 532.67 eV(Table 1). This is in good agreement with the literature values of 529.3–530.3 eV for manganese oxide, 530.3–530.6 eV for vanadium oxide [20, 34], 530.5–531.5 eV for hydroxide, and 531.8–532.8 eV for water [26–32]. The relative percentage of various containing oxygen species was estimated to be 51.03% Mn–O–Mn, 19.23% Mn–O–H, and 29.74% H–O–H for δ-MnO_2. For Mn–V binary oxide,

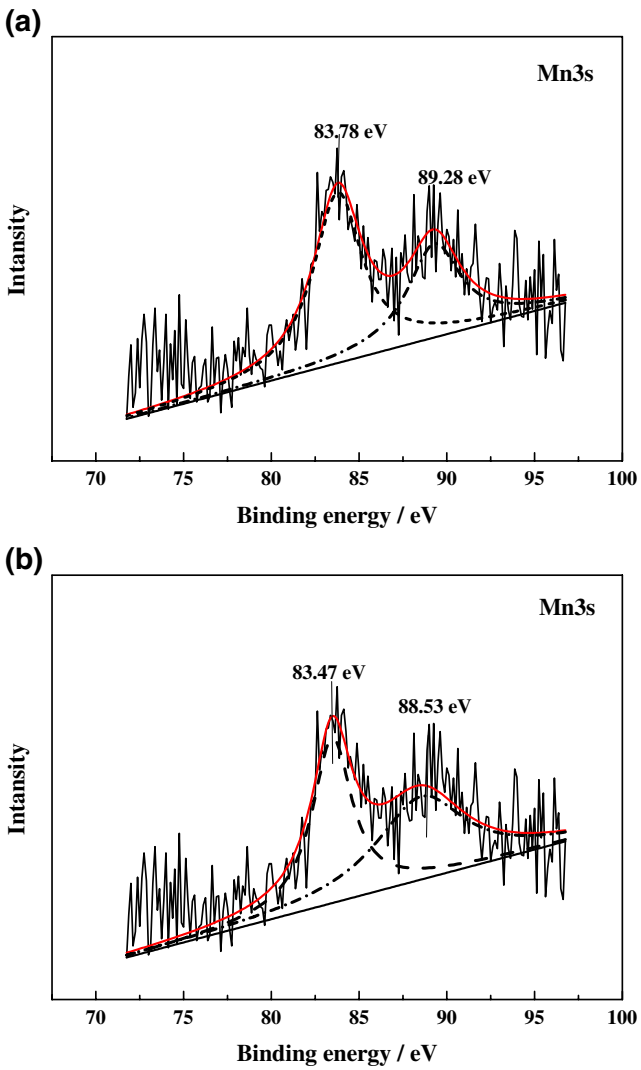

Fig. 5 XPS Mn 3 s spectra of **a** Mn–V binary oxide and **b** δ-MnO_2

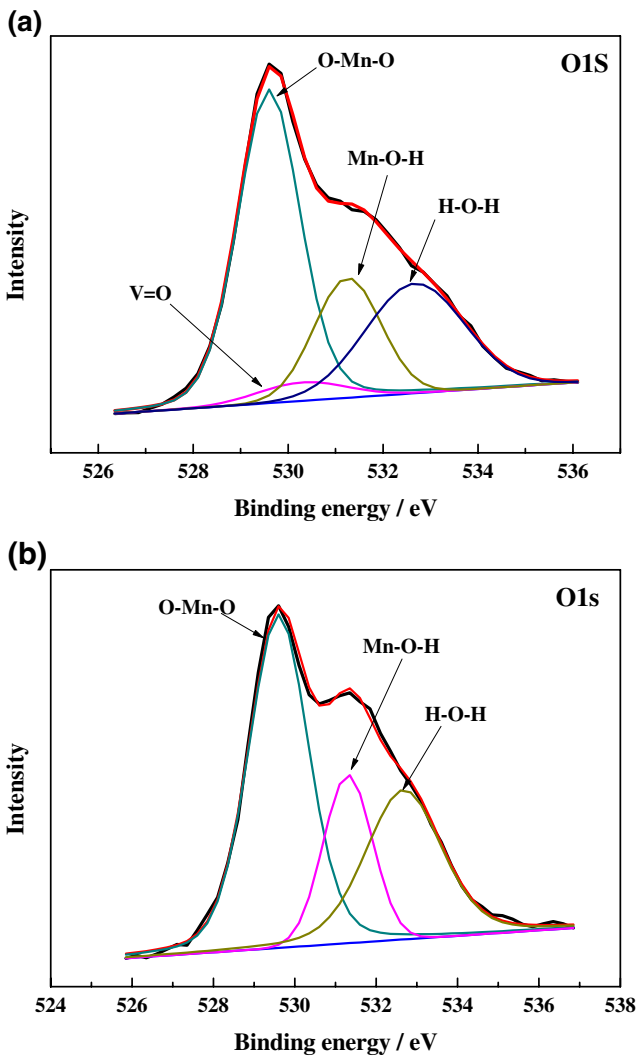

Fig. 6 XPS O 1 s spectra of **a** Mn–V binary oxide and **b** δ-MnO_2

Table 1 XPS data analysis of δ-MnO_2 and Mn–V binary oxide

sample	Mn 2p3/2	Mn 3s			O 1s		Average oxidation state (n)
	BE/eV	BE(1)/eV	BE(2)/eV	ΔE(1–2)/eV	BE/eV	% area	
δ-MnO_2	641.85	88.53	83.47	5.06	529.60	51.03	3.8
					531.57	19.23	
					532.67	29.74	
Mn–V binary oxide	641.75	89.28	83.78	5.5	529.60	50.26	2.5
					530.40	3.90	
					531.60	20.31	
					532.70	25.53	

the relative percentage was estimated to be 50.26% Mn–O–Mn, 3.9% V=O, 20.31% Mn–O–H and 25.53% H–O–H, respectively. Changes in the amount of Mn–O–Mn and H–O–H reveal the effect of adding V_2O_5 on the hydrous nature of MnO_2, in agreement with TGA/DSC studies.

Figure 7a shows the CV of Mn–V binary oxide and δ-MnO_2 in aqueous 0.5 mol L^{-1} Na_2SO_4 electrolyte at a scan rate of 10 mV s^{-1}. It is almost symmetric between the cathode process and anode process within −0.2–1.0 V (vs. SCE), which indicates the good reversibility of the Mn–V binary oxide electrode within −0.2–1.0 V (vs. SCE). But the range for δ-MnO_2 is between 0 and 1.0 V (vs. SCE). This indicates that the applied potential window of composite electrode increased after the incorporation of V_2O_5 into MnO_2 nanostructure. Figure 7b shows that the CV of Mn–V binay oxide at different scan rates. It can be clearly observed that the CV curves are rectangular symmetric at low scan rates within −0.2–1.0 V (vs. SCE). The CV curve exhibits an oblong shape at 40 mV s^{-1}, suggesting that the sample has faster charge transfer and cation diffusion. The value of current response is almost constant. It is almost symmetric between the cathode process and anode process, which indicates the good reversibility of Mn–V binary oxide electrode.

The galvanostic charge–discharge behavior of Mn–V binary oxide was investigated in 0.5 mol L^{-1} Na_2SO_4 solution at 0.25, 0.5, and 1 A g^{-1}, respectively. These constant current charge–discharge curves are shown in Fig. 8a. A linear variation of potential vs. time was observed in all curves, which was another typical characteristic of an ideal capacitor. The calculated specific capacitance for the Mn–V binary oxide electrode at 0.25, 0.5, and 1 A g^{-1} is 335, 322, and 251 F g^{-1}, respectively. But from Fig. 8b, it can be calculated that the specific capacitance of δ-MnO_2 electrode at 0.25, 0.5, and 1 A g^{-1} is 183, 169, and 166 F g^{-1}, respectively.

The electrochemical impedance measurements were carried out on both electrodes. The typical results are shown in Fig. 9. The impedance values (in Ω g^{-1}) are calculated based on the mass of the active MnO_2 or Mn–V binary oxide. Nyquist plots in Fig. 9 show that each impedance spectrum can be generally divided into two regions corresponding to two processes: The high-frequency impedance arc is attributed to the processes

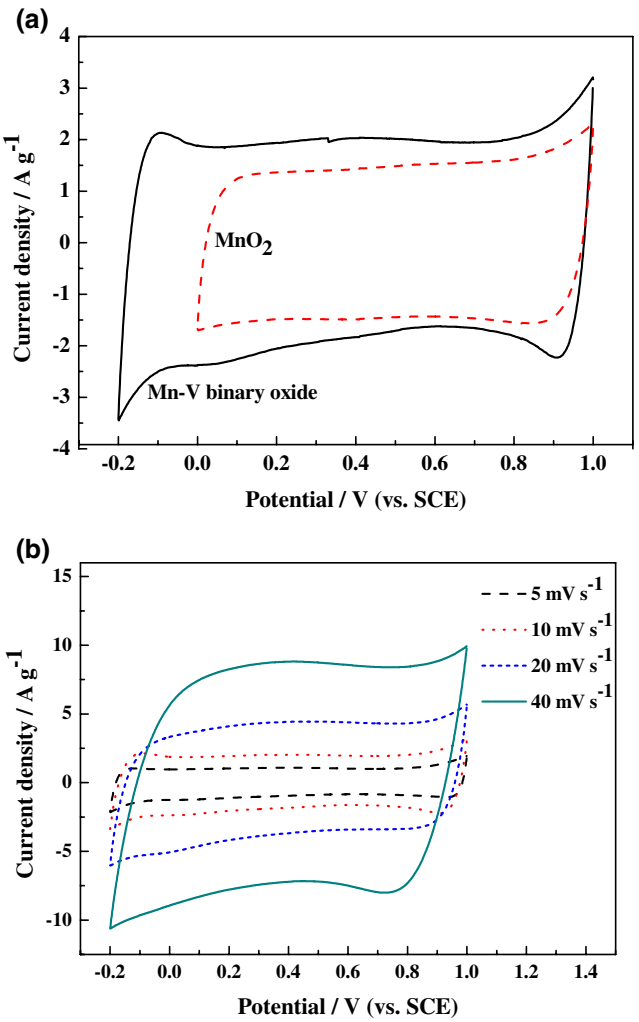

Fig. 7 **a** Cyclic voltammograms of Mn–V binary oxide and δ-MnO_2 in 0.5 mol L^{-1} Na_2SO_4 aqueous electrolyte at room temperature scan rate 10 mV s^{-1}, **b** Cyclic voltammograms of Mn–V binary oxide in 0.5 mol L^{-1} Na_2SO_4 aqueous electrolyte at different scan rate

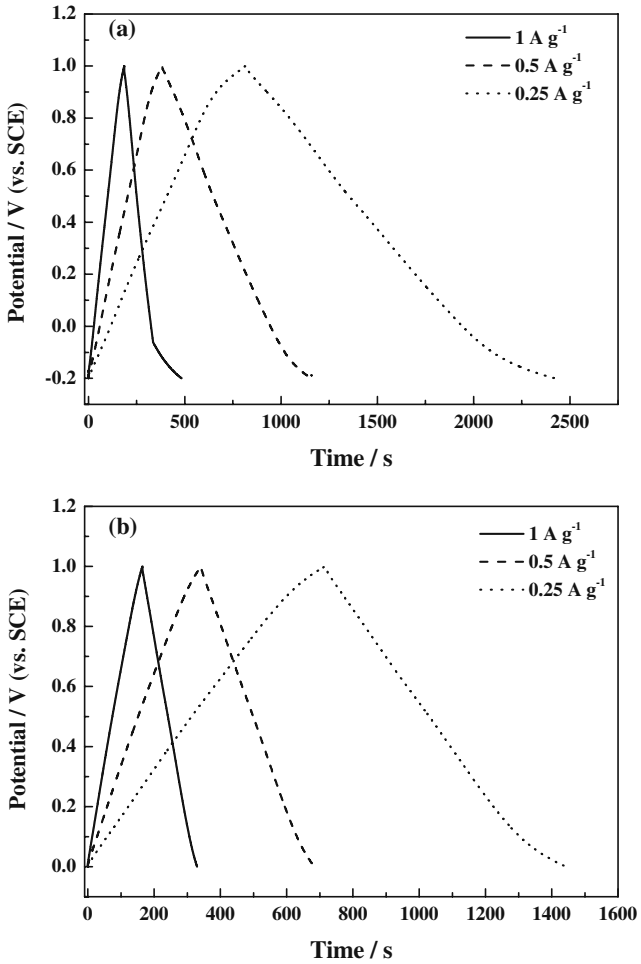

Fig. 8 **a** Galvanostatic charge–discharge curve of Mn–V binary oxide electrode at different discharge current in 0.5 mol L^{-1} Na_2SO_4 aqueous electrolyte, **b** galvanostatic charge–discharge curve of δ-MnO_2 electrode at different discharge current in 0.5 mol L^{-1} Na_2SO_4 aqueous electrolyte

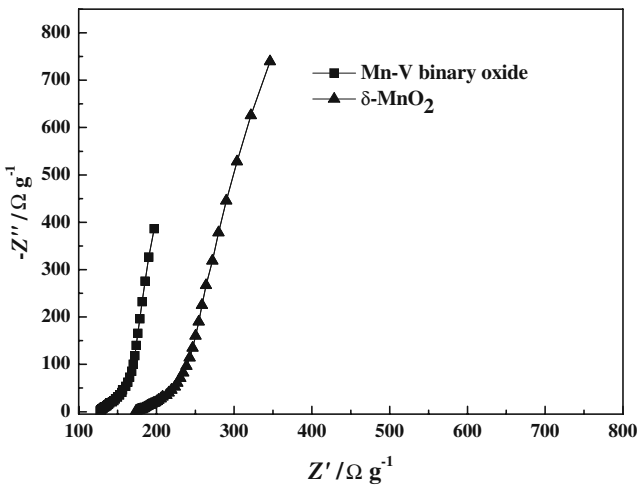

Fig. 9 Nyquist plots of the electrodes **a** Mn–V binary oxide and **b** δ-MnO_2 in 0.5 mol L^{-1} Na_2SO_4 aqueous electrolyte

occurring at the electrode–electrolyte interface [37]. At the low frequency, a line representing a capacitive behavior is clearly found. A major difference in the Nyquist plots is the semicircle in the high-frequency range. It is clear that the Mn–V binary oxide has the lower charge-transfer resistance. The charge-transfer resistance is related to the electroactive surface area of the electrode materials. The larger the electroactive surface area is, the lower the charge-transfer resistance will be [38]. Another difference in the Nyquist plots is the straight line in the low-frequency range. An ideally polarizable capacitance gives rise to a straight vertical line along the imaginary axis (Z''). It indicates that the Mn–V binary oxide has the good capacitance than δ-MnO_2 electrode.

Until now, two mechanisms have been proposed to explain the charge behavior of MnO_2 as active electrode material in aqueous electrochemical supercapacitor [4, 39]. The first one is based on the concept of intercalation of H^+ or alkali metal cations, such as Na^+ in the electrode during reduction and deintercalation upon oxidation

$$MnO_2 + C^+ + e \rightleftarrows MnOOC^+ \quad (2)$$

The second one is the adsorption of cations in the electrolyte on the MnO_2 electrode

$$(MnO_2)_{surface} + C^+ + e \rightleftarrows (MnO_2{}^-C^+)_{surface} \quad (3)$$

Therefore, the physical factors, such as microstructure, surface area, and the chemical factors, such as valence state and hydrous state, may significantly affect the value of specific capacitance [11, 39, 40].

According to the above experimental results, it is suggested that the capacitance performance of Mn–V binary oxides may be improved by following three ways:

1. Small crystalline grain size and large active surface. Some researches indicate that the specific capacitance measured for each MnO_2 phase does not follow the trend of the BET surface area [39, 41]. This conclusion can be obtained when comparing MnO_2 with different crystalline structure. When the electrochemical performance of MnO_2 with same crystalline structure was compared, we believe that the BET surface area is still important factor. This is due to that reaction (3) takes place on the surface of MnO_2. Therefore, the pseudo-capacitance is critically dependent on the effective surface area, which is associated with the crystalline grain size. The large value of BET surface area means that the effective surface area on MnO_2 is larger; therefore the capacitance performance can be improved.
2. Appropriate amount of lattice water. The measurement results of Figs. 3 and 6 confirm that the amount of water for Mn–V binary oxide is less than that for pure δ-MnO_2. It indicates that the amount of water has an

impact on the electrolyte accessibility and diffusion through the MnO_2 material bulk and is related to the intercalation/deintercalation of Na^+. This conclusion is consistent with the reports by Ghaemi et al. [11] and others [12, 30] that the pseudocapacitance depends on the water content in the oxides. But with increasing the water content, the ionic transport increases while the electronic transport decreases. Thus, in order to optimize the performance of the active material, it is necessary to optimize the water content in the oxide by a proper preparation process.

3. Chemical state on the surface of MnO_2 material. According to Toupin et al. [26] and other researchers [27–32], the average oxidation state of Mn for pure MnO_2 is 3.8. On the surface of Mn–V binary oxide, the average oxidation state of Mn is 2.5. It is implied that the capacitance performance will be influenced by chemical state on the surface of MnO_2 materials. Recently, Hu et al. [42] had reported that the activated Mn_3O_4 showed relatively high capacitance (~170 F g^{-1} obtained at 500 mV s^{-1}). Therefore, combining the results of XPS spectra, it could be suggested that the addition of vanadium oxide leading to generate certain amount of Mn_3O_4 is one of the reason for improvement of capacitance performance for Mn–V binary oxide. In addition, the Mn_3O_4 is invisible at XRD. This phenomenon may be cause by following two reasons: (1) the relative sensibility of both methods is different. The relative sensitivity of XRD is 1%, and the relative sensitivity of XPS is 0.1%. If a mere 10^{-7}g of an element can be detected by XPS, the minimum of this element weight that can be analyzed by XRD is 10^{-6}g. (2) When both materials form a solid-solution-kind material, one of the two materials is invisible at XRD. For example, Pt–Ru alloy, Ru element is invisible at XRD [43], and Pt element is visible at XRD. However, Ru oxidation state can be investigated by XPS.

Conclusion

Mn–V binary oxide was successfully synthesized using a novel simple low-temperature precipitation method. The characteristic of Mn–V binary oxide and δ-MnO_2 was investigated by SEM, XRD, TG-DSC, XPS, CV, galvanostatic charge/discharge curve, and EIS. The result indicated that the specific capacitance increased from 166 F g^{-1} estimated for δ-MnO_2 to 251 F g^{-1} for Mn–V binary oxide and the applied potential window of binary oxide electrode increased after the incorporation of V_2O_5 into δ-MnO_2 structure. The surface area of the mixed oxide increased due to the formation of small grain size and particle size. The TG/DSC and XPS studies showed that the change in the crystalline structure and the mixed oxide decomposition process and chemical state on the surface led to the increase of capacitance in the case of Mn–V mixed oxide. The capacitance performance of Mn–V binary oxide may be improved by following three factors: (1) small grain and particle size and large activity surface area, (2) appropriate amount of lattice water, and (3) chemical state on the surface of MnO_2 material.

Acknowledgment Financial support for this work was provided by Major State Basic Research Development Program (no. 2008CB617502).

References

1. Bagotsky VS (2006) Fundamentals of electrochemistry. Wiley, New York
2. Lazzari M, Soavi F, Mastragostino M (2009) J Electrochem Soc 156:A661–A666
3. Changa KH, Hua CC, Chou CY (2009) Electrochim Acta 54:978–983
4. Athouél L, Moser F, Gugas R, Crosnier O, Blanger D, Brousse T (2008) J Phys Chem C 112:7270–7277
5. Chen L, Yuan C, Gao B, Chen S, Zhang X (2009) J Solid State Electrochem 13:1925–1933
6. Qu QT, Shi Y, Li LL, Guo WL, Wu YP, Zhang HP, Guan SY, Holze R (2009) Electrochem Comm 11:1325–1328
7. Xiao W, Xia H, Fuh JYH, Lu L (2009) J Power Sources 193:935–938
8. Reddy RN, Reddy RG (2003) J Power Sources 124:330–337
9. Devaraj S, Munichandraiah N (2008) J Solid State Electrochem 12:207–211
10. Yuan AB, Wang ML, Wang YQ, Hu J (2009) Electrochim Acta 54:1021–1024
11. Ghaemi M, Ataherian F, Zolfaghari A, Jafari SM (2008) Electrochim Acta 53:4607–4614
12. Kim H, Popov BN (2003) J Electrochem Soc 150:D56–D62
13. Lee MT, Chang JK, Hsieh YT, Tsai WT (2008) J Power Sources 185:1550–1556
14. Machefaux E, Brousse T, Bélanger D, Guyomard D (2007) J Power Sources 165:651–655
15. Nakayama M, Tanaka A, Konishi S, Ogura K (2004) J Mater Res 19:1509–1515
16. Chen LM, Lai QY, Hao YJ, Zhao Y, Ji XY (2009) J Alloys Compd 467:465–471
17. Zolfaghari A, Ataherian F, Ghaemi M, Gholami A (2007) Electrochim Acta 52:2806–2814
18. Ragupathy P, Park DH, Campet G, Vasan HN, Hwang SJ, Choy JH, Munichandraiah N (2009) J Phys Chem C 113:6303–6309
19. Cullity BD, Stock SR (2001) Element of X-ray diffraction. Prentice-Hall, New Jersey
20. Khyzhuna OY, Strunskus T, Grünert W, Wöll C (2005) J Electron Spectrosc Relat Phenom 149:45–50
21. Yuan A, Wang X, Wang Y, Hu J (2009) Electrochim Acta 54:1021–1026
22. Donkova B, Mehandjiev D (2004) Thermochim Acta 421:141–149
23. Devaraj S, Munichandraian N (2007) J Electrochem Soc 154: A80–A88
24. Yuan A, Zhang QL (2006) Electrochem Commun 8:1173–1178
25. Xu Q, Zhao K, Gu C (2002) Chinese J Rare Metal 26:169–172
26. Toupin T, Brousse T, Bélanger D (2002) Chem Mater 14:3946–3952

27. Nagarajan N, Cheong M, Zhitomirsky I (2007) Mater Chem Phys 103:47–53
28. Chang JK, Chen YL, Tsai WT (2004) J Power Sources 135:344–353
29. Subramanian V, Zhu H, Vajtai R, Ajayan PM, Wei B (2005) J Phys Chem B 109:20207–20214
30. Chang JK, Tsai WT (2003) J Electrochem Soc 150:A1333–A1338
31. Wei W, Cui X, Chen W, Ivey DG (2009) J Power Sources 186:543–550
32. Yan D, Yan P, Cheng S, Chen J, Zhuo R, Feng J, Zhang G (2009) Cryst Growth Des 9:218–222
33. Strohmeier BR, Hercules DM (1984) J Phys Chem 88:4922–4929
34. Nguyen TD, Do TO (2009) Langmuir 25:5322–5332
35. Chigane M, Ishikawa M (2000) J Electrochem Soc 147:2246–2251
36. Chigane M, Ishikawa M, Izaki M (2001) J Electrochem Soc 148: D96–D101
37. Gamby J, Taberna PL, Simon P, Fauvarque JF, Chesneau M (2001) J Power Sources 101:109–116
38. Wu MS, Huang YA, Yang CH (2008) J Electrochem Soc 155: A798–A805
39. Devaraj S, Munichandraiah N (2008) J Phys Chem C 112:4406–4417
40. Chang JK, Huang CH, Lee MT, Tsai WT, Deng MJ, Sun IW (2009) Electrochim Acta 54:3278–3284
41. Ghodbane O, Pascal JL, Favier F (2009) Appl Mater Inter 1:1130–1139
42. Hu CC, Wu YT, Chang KH (2008) Chem Mater 20:2890–2894
43. Lin ML, Lo MY, Mou CY (2009) J Phys Chem C 113:16158–16168